Advanced Functional Materials

ADVANCED FUNCTIONAL MATERIALS
www.afm-journal.de

RESEARCH ARTICLE OPEN ACCESS

Dispensing Volumetric Additive Manufacturing

Hongryung Jeon[1] | Yunsoo Lee[1] | Seobin Park[1] | Kyung-Hwan Kim[1] | Junyoung Seo[1] | Im Doo Jung[1,2]

[1]Department of Mechanical Engineering, Ulsan National Institute of Science and Technology (UNIST), Ulsan, Republic of Korea | [2]Artificial Intelligence Graduate School, Ulsan National Institute of Science and Technology (UNIST), Ulsan, Republic of Korea

Correspondence: Im Doo Jung (idjung@unist.ac.kr)

Received: 30 November 2025 | **Revised:** 9 March 2026 | **Accepted:** 17 March 2026

Keywords: computed axial lithography | dispensing based fabrication | high-throughput manufacturing | tomographic photopolymerization | volumetric additive manufacturing

ABSTRACT

Despite the advantages of additive manufacturing (AM) in creating customized 3D shapes, conventional layer-by-layer approaches are limited by low production rates, restricting their broader applications. Volumetric additive manufacturing (VAM) has emerged as a promising technique, enabling the simultaneous photopolymerization of entire volumes, which significantly reduces fabrication time. However, current computed axial lithography requires manual operations per print cycle, such as loading resin into a vial, physically placing and aligning the vial (with or without an index-matching medium), and removing the printed object, limiting continuous, high-throughput production of multiple parts. Here, we propose a dispensing volumetric additive manufacturing (DVAM) method that prints and dispenses each part within a droplet in less than a minute. The printing process occurs within a single droplet dispensed from a glass pipette, enabling simultaneous printed object removal and resin replenishment in a second. Light pattern distortion caused by the absence of the index-matching fluid was corrected through real-time droplet profile estimation and inverse ray-tracing within the optical system. We demonstrate rapid serial VAM of 10 different objects within 10 min. This approach establishes a practical pathway toward scalable, high-throughput volumetric manufacturing, enabling rapid production of complex 3D structures without the operational bottlenecks of conventional VAM workflows.

1 | Introduction

3D printing, also known as additive manufacturing (AM), has become a transformative fabrication strategy across diverse fields, including healthcare and medical devices, aerospace and automotive engineering, electronics, and soft robotics, largely because it enables the creation of complex geometries with minimal tooling [1–7]. However, most existing 3D printing platforms rely on point-by-point or layer-by-layer deposition. Because each line or layer must be written sequentially, the total fabrication time inevitably scales with object size, height, and geometric complexity. This inherent sequential processing imposes fundamental limits on printing speed and has motivated the development of approaches that can overcome the throughput bottlenecks of layer-based manufacturing. Light-based AM techniques, such as SLA and DLP, enable smooth surface quality and micron-scale resolution, which have advanced bioprinting and tissue engineering applications [8–11]. However, photopolymerization-based lithographic methods exhibit a trade-off between feature resolution and production rate. Enhancing resolution generally requires a substantial increase in the number of discrete slice images and the precision of projected patterns, thereby prolonging fabrication time. For example, projection stereolithography conventionally requires an approximately 5–10× decrease in production rate to achieve a twofold improvement in millimeter- or micron-scale resolution [12]. This trade-off highlights the mismatch between print speed and achievable throughput in conventional layer-by-layer processes compared to VAM (Figure S10).

Volumetric additive manufacturing (VAM) has emerged as a compelling alternative by reversing the conventional printing paradigm. Instead of constructing objects layer by layer, VAM solidifies material throughout an entire 3D volume simultaneously by using computed light fields [13]. This volume-wide exposure decouples print time from object height and minimizes mechanical motion, enabling the rapid fabrication of intricate, free-standing structures. Techniques such as computed axial lithography (CAL) and xolography have demonstrated the ability to generate complex geometries across diverse resin systems, highlighting the speed and geometric freedom afforded by volumetric exposure [14–26].

Despite these advantages, current VAM implementations present operational limitations that impede the rapid and continuous production of multiple parts. Most CAL-based systems require a dedicated cylindrical container filled with resin, an index-matching fluid to maintain uniform illumination, and manual extraction of the printed object after curing. Once the object is removed, the container must be refilled or replaced before the next print can begin. These repeated preparations and clearing steps interrupt production and prevent continuous multi-object fabrications. Continuous variants of 3D printing, such as flow lithography and flow-enabled xolography, aim to maintain a refreshed resin environment and reduce downtime between prints [27–32]. However, these approaches typically require large volumes of flowing resin, which increases material consumption and introduces challenges related to flow stability, optical uniformity, and resin replenishment. Consequently, although VAM can fabricate a single object rapidly, existing systems struggle to translate this intrinsic speed into high-throughput, sequential manufacturing.

Here, we introduce a dispensing-based VAM approach in which 3D structures are formed directly within a resin droplet suspended from a glass pipette. In this configuration, a pendant droplet naturally serves as a confined printing volume, and volumetric illumination during rotation enables uniform solidification throughout the resin without the need for a container, flow cell, or index-matching medium. After printing, the cured structure is dispensed, and the next droplet immediately provides a fresh, self-contained volume for subsequent fabrication. By allowing each droplet to function as a temporary and automatically replenished reaction chamber, this approach supports the rapid serial production of multiple parts while eliminating the preparation and clearing steps inherent to VAM workflows.

2 | Results and Discussion

Figure 1a illustrates the dispensing volumetric additive manufacturing (DVAM) process, in which a single resin droplet is dispensed from a glass pipette and serves as the confined printing volume. The system employs a modulated projection scheme that selectively polymerizes the photocurable resin within the droplet. The resin contains a monomer-photoinitiator mixture that undergoes polymerization when exposed to tomographically computed light patterns. During rotation, the resin adheres to the pipette tip and is directly illuminated by the tomographic projections generated by the digital micromirror device (DMD).

In conventional CAL, the resin is placed inside a rectangular chamber filled with an index-matching fluid to ensure that the projection light enters without distortion. In contrast, instead of utilizing an index-matching fluid, this system employs a droplet-based configuration that enables both resin supply and printed-part release through simple dispensing after polymerization. However, the curved resin-air interface introduces lensing effects and image distortions, thereby necessitating the application of a sophisticated refractive correction process to mathematically compensate for these optical deviations. Our approach utilizes a contro divergent beam from an aperture to counteract the inherent convergence of the vial-resin interface for the projected patterns throughout the resin volume. To implement this concept, we constructed a CAL platform for rapid serial fabrication that streamlines the pre- and post-printing processes (Figure 1b). A syringe and glass pipette were mounted on a rotation stage, and pendant droplets were generated at the pipette tip by applying pressure to the pre-filled syringe. A supporting structure was added to minimize vibration and lateral motion, ensuring stable rotation during exposure. The optical system consists of a 442 nm laser diode, a square-core optical fiber, a DMD, and multiple optical components, enabling the photomask to be positioned within a few millimeters of the resin droplet. The optical path is designed so that the modulated beam is efficiently coupled, collimated, and uniformly delivered onto the pendant droplet.

The droplet remains stable throughout exposure due to the high viscosity of the resin, allowing targeted geometries to be fully polymerized within the confined volume (Movie S1). The total printing time ranges from approximately 45–75 s, after which the cured object detaches and is dispensed onto a moving substrate (Figure 1c). By repeating the printing cycle, multiple structures can be fabricated in a streamlined sequence. After each tomographic exposure, the printed object, still carrying uncured resin, naturally separates from the pipette tip and is deposited onto the substrate, while fresh resin is immediately supplied by applying syringe pressure to form the next droplet.

The DVAM process enables high-repeat rate fabrication, in which droplet formation, volumetric printing, and dispensing occur in a repetitive loop (Figure 2a). Real-time CCD monitoring confirms uninterrupted printing and release cycles for various representative geometries (Figure 2b). The system is configured so that printed objects are automatically transferred to the cleaning stage, where uncured resin is removed. In Movies S2 and S3, a thin layer of washing liquid is applied to the substrate surface to enhance visualization of the printing dynamics inside the pendant droplet. This optical arrangement allows clear recording of the entire droplet profile and its detachment behavior, revealing the transition from the pendant state to the release phase.

The pendant droplet exhibits a characteristic equilibrium shape governed by the wetting properties of the liquid [33]. In the DUDMA/TMPTA resin mixture, the droplet maintains an elongated morphology before detaching from the pipette tip (Figure S1). Analysis of the droplet profile and quantitative evaluation of the angular deviation of the transmitted light allow identification of the printable region within the droplet. The maximum droplet height z_{max} and the contact angle θ_c at the pipette wall arise from the balance between gravitational and surface tension forces acting on the dispensed volume (Figure 3a). The relationship

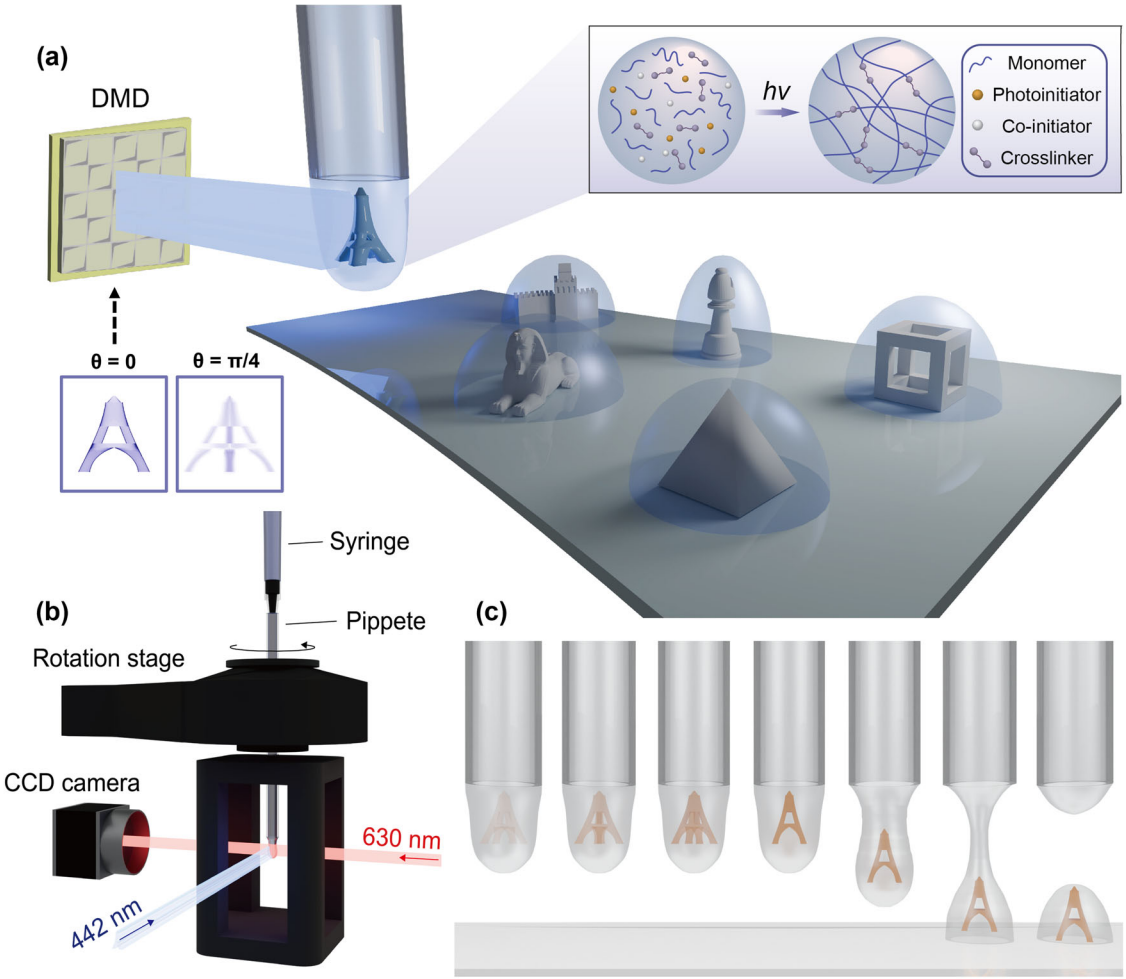

FIGURE 1 | (a) Schematic of the droplet-based rapid serial printing approach of computed axial lithography. Photocurable resin is selectively polymerized by tomographic patterns. The laser-driven light pattern projected onto the DMD is optically corrected to ensure precise printing due to the refractive index-matching fluid. (b) Experimental setup for droplet-based VAM, using a laser diode (442 nm) for polymerization and a red (630 nm) LED source for CCD monitoring. (c) Schematic of droplet formation and printing sequence. Tomographic light patterns cure the target geometry, after which the printed object is dispensed onto the moving substrate.

between θ_c and z_{max} shows that the contact angle θ_c increases at smaller droplet volumes, where surface tension dominates (Figure 3b). For a 3 mm pipette, the contact angle exceeds 90°, indicating that surface tension suppresses wetting of the wall at low volume. As the dispensed volume increases, gravitational forces become more influential, causing the droplet to elongate and the contact angle to decrease accordingly.

To achieve optical exposure with minimal distortion on a curved droplet along the *z*-axis, the transmitted angle is determined using ray-tracing. The transmitted angle (θ_t) is defined as the angle between the transmitted light path and a reference line (dashed line in Figure 3a) parallel to the *z*-axis. The printable region is defined as the zone where the transmission angle lies between 85° and 95°, corresponding to light-path deviations of only a few tens of micrometers. An optical image of the pendant droplet is first acquired at its maximum resin volume under 630 nm illumination. The curved droplet boundary is extracted using binarized thresholding and fitted to obtain the radial profile r(z) (Figure S2). This profile is then used as the geometric input for ray-tracing calculations performed at each point on the droplet interface to determine the refracted optical path (Note S1). The 4 mm pipette provides a maximum printable height of approximately 2.8 mm (Figure 3c) and was used for all printing. When resin is contained in a cylindrical vial, the fluid undergoes solid-body rotation in which all elements exhibit uniform angular velocity at the container boundary. The pendant droplet attached to the pipette tip exhibits the same uniform angular velocity condition, which is established within 40 ms as verified by simulation (Figure S3).

A refractive correction strategy was implemented to compensate for the optical distortions that occur at the air-resin interface due to the refractive index mismatch and the deformed geometry of the pendant droplet. To satisfy telecentric illumination conditions, we calculate the incident angle and spatial coordinates of each ray by modeling them as originating from a canonical telecentric plane, which serves as a computational proxy for an ideal telecentric source [34, 35]. This mapping allows the system to precisely determine the correspondence between the physical DMD coordinates and their counterparts. To achieve this correction, the droplet geometry is first detected in real time using

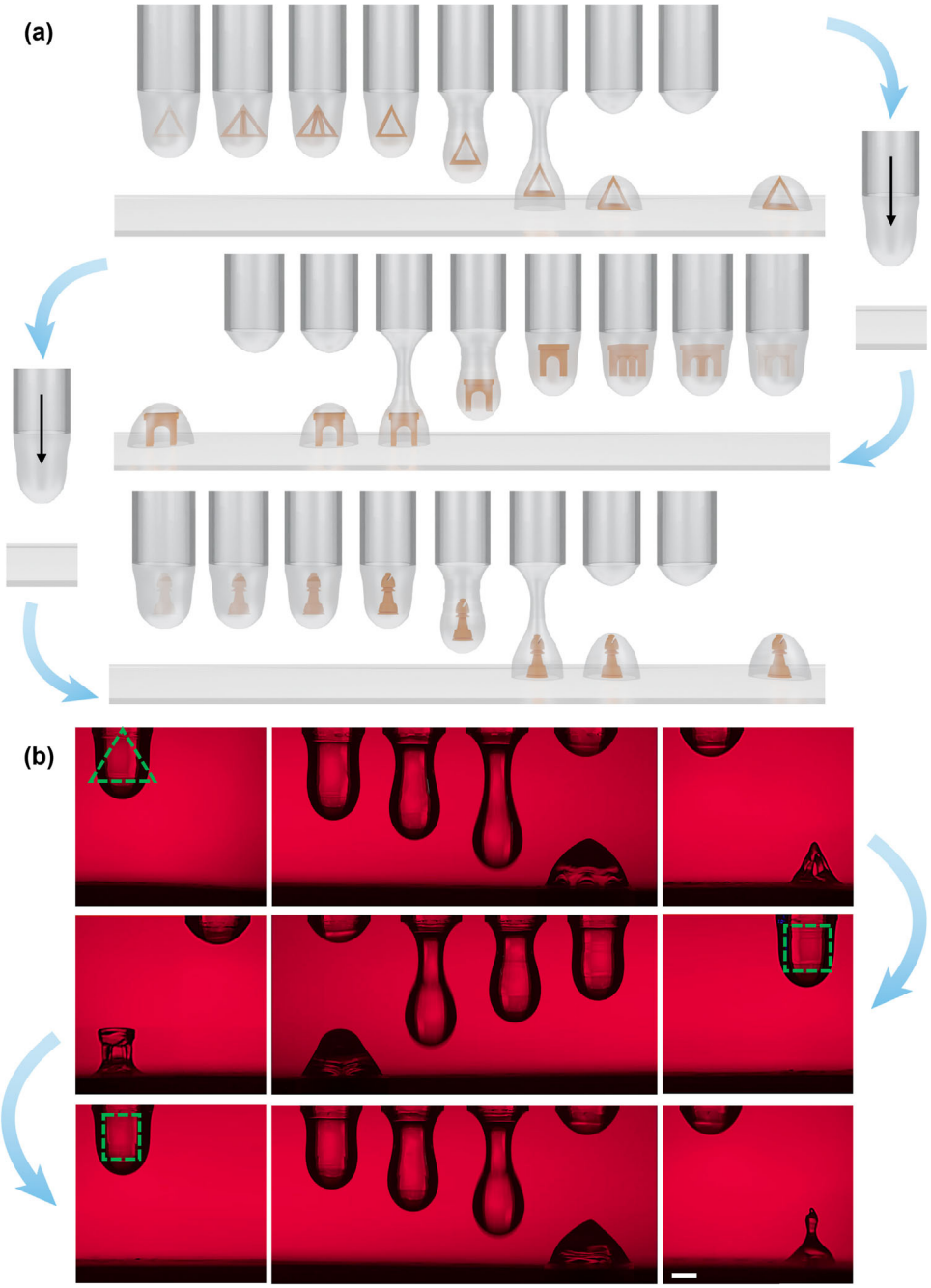

FIGURE 2 | Rapid serial fabrication process in dispensing-based VAM. After curing, the droplet is detached from the pipette, and the solidified 3D structure is deposited onto the substrate. A fresh pendant drop is subsequently generated for the next printing cycle. (a) Schematic and (b) real-time CCD images of the droplet formation, exposure, detachment, and deposition stages for several shapes (hollow pyramid, arch, and bishop). The scale bar is 1 mm.

a CCD camera, since small variations arise with each dispensing event, and the resin-air boundary is extracted through threshold-based image segmentation. The resin-air interface is identified in each frame and referenced to the centroid of the pendant droplet to account for lateral motion during image processing. During printing, the droplet centroid is tracked to quantify wobble and to robustly extract the droplet profile; the projection coordinate system is set to the droplet via a camera-projector calibration performed upon droplet formation. Frame-to-frame centroid tracking indicates a residual lateral wobble of ~25 μm (occasionally up to ~50 μm), which is not negligible relative to the smallest demonstrated feature size (~150 μm) and may contribute to feature rounding. Nevertheless, this correction strategy effectively suppresses first-order translational misalignment and enables consistent reconstruction of the overall geometry and reliable comparison of printing fidelity across conditions, particularly for millimeter-scale structures. The intended coordinates at the center of the resin are then estimated, and inverse ray tracing is applied to determine the corresponding projection coordinates on the DMD (Figure 3d). This entire workflow is automated using an AI-based droplet detection system built on a customized YOLO framework, which we retrain and tune to robustly identify

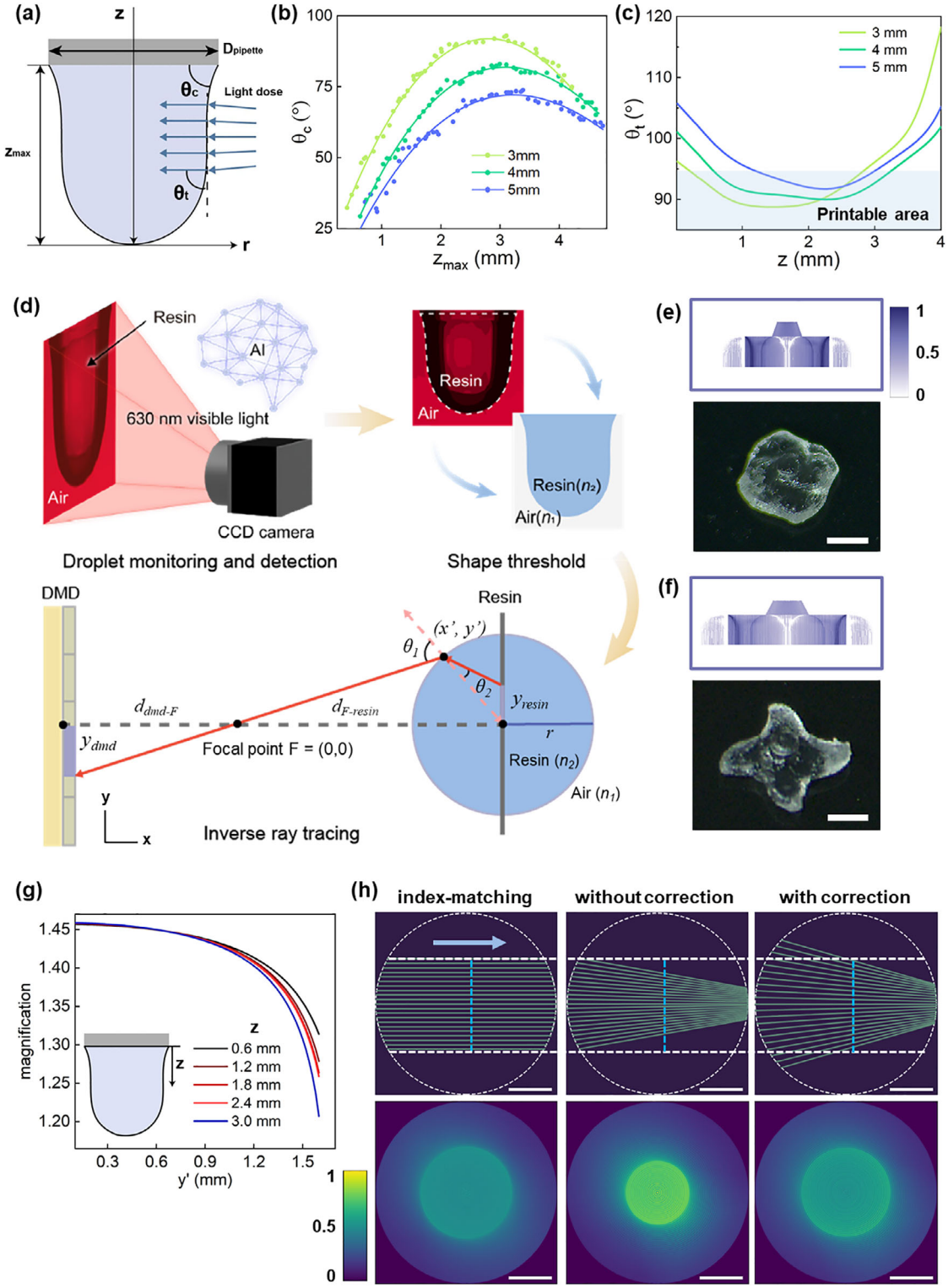

FIGURE 3 | Characteristics of pendant drop and pattern correction. (a) Illustration of the pendant drop. As the resin is dispensed, the droplet shape is governed by the resin properties and the diameter of the glass pipette, which determine the contact angles (θ_c) and the droplet height (z_{max}). This affects the transmitted angle (θ_t) when the light dose is projected onto the surface. (b) Variation of the height of the pendant drop with the contact angle for different $D_{pipette}$ (3, 4, 5 mm) when resin is gradually dispensed. Each datapoint represents an experimental measurement, and all points are fitted as curves. (c) Graph of the transmitted angle for the pendant drop. (d) Schematic of the correction process from the droplet shape detection by the CCD camera. Projection images with normalized intensity scale and prints for the rotor shape (e) before and (f) after correction. The scale bar is 500 μm. Projection images with pixel-wise correction are applied, demonstrating spatial magnification across the object. (g) Magnification (y'/y_{resin}) plots as a function of radial distance (r) for each droplet height from the pipette tip, illustrating nonlinear distortion in the optical path. The magnification tends toward the resin edge, with differences observed across droplet heights due to variations in surface radius. (h) Accumulated dose map for ray tracing after rotation (with index-matching fluid, without correction, and with correction). The scale bar is 400 μm.

the resin droplet across varying illumination conditions and droplet geometries [36]. The AI model provided precise, frame-by-frame localization and contour extraction, enabling accurate computation of the radial profile r(z) from the segmented droplet shape.

Using the extracted droplet geometry, we performed a comprehensive optical mapping to determine the final DMD patterns. Each ray was numerically traced using Snell's law to account for refraction at the curved resin-air interface, establishing an exact correspondence between the physical DMD coordinates and the canonical telecentric plane (Algorithm S1 and Figure S5). A critical consideration in this process is the non-uniform energy dose distribution resulting from light convergence. Because the convex droplet acts as a lens, optical intensity can be locally concentrated, potentially leading to overcuring. To ensure a uniform delivered energy dose throughout the rotating resin volume, we integrated an intensity compensation step into the forward mapping, in which pixels corresponding to regions of high optical convergence were assigned reduced intensities. This correction was iteratively applied across all projection angles of the tomographic dataset for 3D reconstruction. Unlike previous refraction-correction approaches developed for cylindrical resin containers, the present framework is formulated for a pendant droplet geometry with a curved resin-air interface and incorporates both geometric correction and energy-dose compensation to address curvature-induced ray convergence.

Figure 3e,f highlights the impact of this correction on printing accuracy using a rotor structure with tip features. Without correction, the projection images resemble those used in conventional CAL, producing prints with rounded contours and poorly defined tips that deviate substantially from the intended design. With refractive correction, the projection images undergo magnification determined by the curvature of the air-resin interface, and the printed structure accurately reproduces the well-defined tips of the target geometry. The magnitude of this correction is quantified by the magnification, defined as the distance ratio (y'/y_{resin}) between the projection formed at the droplet interface and the corresponding coordinate at the resin center. In the DUDMA/TMPTA resin, which has a refractive index of 1.488, the magnification is approximately 1.45 near the *x*-axis and gradually decreases toward the droplet edges (Figure 3g). Light dose mapping further illustrates the effectiveness of the strategy. Three cases were compared: an ideal index-matched configuration, the uncorrected projection, and the refractive-corrected projection (Figure 3h). Index-matching fluid produces parallel ray shifts and an evenly distributed dose profile, serving as the reference condition. The corrected projection was computed so that each light dose reaches the same spatial locations as in this ideal case, resulting in an effective dose diameter reaching up to 96 % of the index-matched condition with a similar distribution. In contrast, uncorrected projections converge laterally toward the center, producing a normalized dose profile that spans only about 66 % of the target diameter, with a strong concentration of light at the center. This observed coverage is attributed to the refractive index ratio ($n_{air}/n_{resin} \approx 0.672$, $n_{air} \approx 1$, $n_{resin} \approx 1.488$) between the droplet and air. These dose distributions, with the printing results, validate that the refractive correction strategy effectively compensates for the geometric distortion of the droplet and enables faithful reproduction of the intended structure.

The CAL method employs rotation speeds of approximately 60° s^{-1}, depending on resin composition and printer configuration [21]. Local solidification within the resin volume is contingent upon the depletion of oxygen. In acrylate polymerization, rotation speed does not directly alter intrinsic reaction rate constants, but instead regulates the temporal exposure profile and the balance between radical generation and oxygen inhibition. As a result, the polymerization response can appear nonlinear, particularly under spatially varying or converging light fields where local intensity differences and oxygen depletion dynamics are amplified [15, 37]. Figure S7 shows the fabrication of pyramid structures with target square-base dimensions (S_Δ) of 1×1 and 2×2 mm^2 at rotation speeds (v_r) of 6, 12, 18, and 24° s^{-1}. For the larger base size of 2×2 mm^2, structurally stable pyramids were obtained at 12–24° s^{-1}. The time required for the base to reach its designed dimension decreased from 58 s at 24° s^{-1} to 52 s at 12° s^{-1} (Figure 4c). At 6° s^{-1}, the total printing time was further reduced to 48 s, although slight feature merging appeared near the apex. This indicates that at low rotation speeds, incomplete rotational averaging allows local dose accumulation to exceed the polymerization threshold within a partial rotation, leading to the observed distortion and reduced resolution. This behavior is attributed to the spatially non-uniform instantaneous light intensity and polymerization-induced resin shrinkage during curing [38]. Although the integrated dose is designed to be uniform, the converging light field produces position-dependent intensity, causing regions exposed to higher intensities to exceed the polymerization threshold earlier. Under low rotation speeds, the prolonged dwell time accelerates local solidification and subsequent resin shrinkage, allowing those regions to stabilize at the designed dimensions earlier than regions exposed to lower instantaneous intensities. For the smaller $S_\Delta = 1 \times 1$ mm^2 structures, printing time showed a modest reduction from 64 to 61 s at lower v_r. The influence of rotation speed is further quantified by Jaccard index (Intersection over Union, IoU) values extracted from the stacked images of micro-CT (Figure 4d). For $S_\Delta = 2 \times 2$ mm^2, IoU values exhibited, 89.07 % ± 1.77 % at 24° s^{-1} and 76.68 % ± 1.53 % at 6° s^{-1}, indicating minimal sensitivity to rotation. In contrast, for the 1×1 mm^2 structures, IoU dropped markedly to 52.28 % ± 1.07 % at 6° s^{-1}, consistent with non-uniform polymerization for the entire shape and insufficient rotation. Based on these results, a rotation speed of 24° s^{-1} was selected for the fabrication of all subsequent structures presented in this work, as it provides the highest and most consistent printing fidelity across feature sizes. While higher rotation speeds could further improve angular averaging, the maximum attainable speed of the precision rotation stage in our system is 25° s^{-1}. Moreover, we observe that the fidelity approaches a plateau near 24° s^{-1}, indicating diminishing improvement beyond this value. Therefore, 24° s^{-1} represents a practical and optimal operating condition balancing fidelity and hardware constraints.

Figure 4a compares the geometric fidelity of 2.5D and 3D structures printed with and without refractive correction, using identical exposure times. Uncorrected prints exhibit distorted or incomplete geometries, whereas corrected prints reproduce the intended shapes. Corrected cubes and square pyramids display edges and maintain height-to-width ratios of 1:1.02 and 1:1.06, respectively, in close agreement with CAD designs. Without correction, rounded edges and incomplete triangular facets are observed, resulting in reduced ratios of 1:0.73 and 1:0.76. In

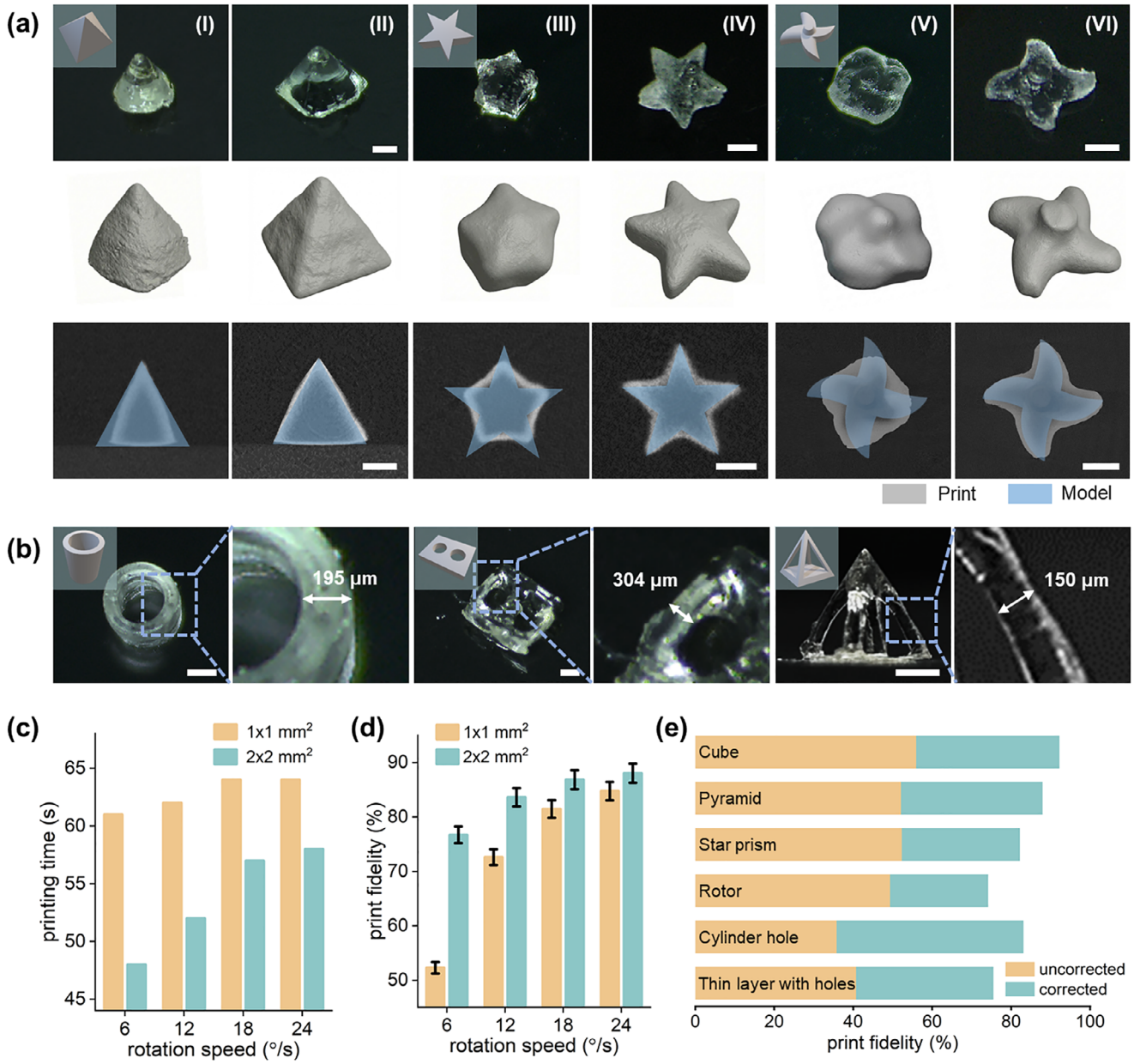

FIGURE 4 | Printability for pendant drop computed axial lithography. (a) Optical images, 3D micro-CT cross-sections, and shapes show the comparison of 2.5D and 3D geometries (I, III, V: without correction, II, IV, VI: with correction. Pyramid, Star prism, Propeller. The scale bar is 500 µm. For each geometry, the 3D reconstructed volumes and corresponding cross-sectional slices are presented for both uncorrected and corrected prints. In the cross-sectional views, the micro-CT data (gray) is overlaid with the target CAD design (blue). (b) Microscale features for Cylinder hole, Thin layer with holes, and Hollow square pyramid. (c) Graph of printing time for the same dimensions of the pyramid shape with different rotation speeds. The printing time is measured when the bottom square reaches the target dimensions. (d) The fidelity graph between the designed and printed shapes varies with the rotation speed. Print fidelity measured as the Jaccard index, or 3D intersection over union (IoU), computed from micro-CT image stacks. Error bars indicate standard error. (e) Print fidelity for each shape was also measured as IoU from micro-CT between the CAD and the print. The scale bar is 500 µm.

more complex geometries, such as star prisms and propeller structures, uncorrected prints show severe inward merging of tip or blade features toward the central axis. In the cross-sectional view, the star prism deviates notably from the target pentagonal form, forming shallow indentations instead of tips. Figure 4b illustrates the fabrication capabilities of microscale features in this system. A triangular pyramidal lattice structure was printed with a base dimension of 1.5 mm, and the minimum feature size within the lattice beams was approximately 150 µm. The printed lattice exhibited a well-defined 3D outline, and the narrow beam elements were reproduced with consistent clarity, reflecting the characteristic dimensions of the target design.

Jaccard Index analysis (Figure 4e) shows that corrected cubes and pyramids achieve IoU values of 92.18 % and 88.93 %, whereas uncorrected prints reach only 55.89 % and 52.04 % due to refractive-index-induced demagnification of the light path. These values align with the theoretical dimensional deviations expected

based on the resin's optical properties. Corrected star and rotor structures achieve IoU values of 83.16 % and 74.14 %, respectively. The improvement is particularly pronounced in hole bearing geometries: uncorrected prints of the cylinder hole and thin layer hole structures yield IoUs of 35.76 % and 40.66 %, respectively. These results demonstrate that the applied correction strategy, based on inverse ray tracing and angular compensation in the mask design, effectively restores the geometrical accuracy of features across the build volume, especially at the periphery where refractive distortion is most severe.

In pendant drop volumetric printing, the implementation of computational correction ensures that the dispensing-based volumetric approach maintains spatial fidelity of the light exposure. This enables the precise fabrication of complex 3D structures with high printability. Overall, the findings demonstrate that the process effectively bridges the gap between precise volumetric printing and practical design implementation with minimal non-printing overhead. CAL inherently enables the formation of internal voids, thin walls, and negative geometries, and the introduction of droplet-based volumetric printing extends these capabilities while substantially reducing non-printing overhead. These results demonstrate that DVAM can reliably generate CAL-resolution structures in rapid, repeated cycles, increasing its practicality for applications requiring fast prototyping of multiple complex 3D shapes.

Figure 5 summarizes the core performance of the DVAM platform. The left panels present sequential CAD models and their corresponding printed structures arranged on the moving substrate with a rotation speed of 24° s^{-1}. The selected geometries include lattices, overhangs, hollow features, high-curvature bodies, and freeform shapes, allowing comprehensive assessment of 3D fidelity. The final row includes the "A B C D E U N I S T" letter sequence, demonstrating the ability to fabricate distinct structures in uninterrupted succession. All prints were produced using a 4 mm pipette at a rotation speed of 24° s^{-1}. Each droplet was exposed volumetrically for 45–75 s and released onto the moving substrate before the next droplet was dispensed, illustrating the rapid serial nature of the workflow without reservoir replacement or mechanical part removal. The rounded appearance of fine features in the present DVAM implementation is primarily associated with mechanical stability and concentric alignment limitations of the current laboratory-built setup, which can lead to small frame-to-frame misregistration between the projected patterns and the rotating pendant droplet with the restricted build volume. Minor light-path deviations of several degrees can also lead to positional offsets on the order of a few tens of micrometers. Further improvements in mechanical stabilization, alignment, and optimized aperture configuration for the small, curved resin volume are expected to reduce residual wobble and improve feature-level geometric fidelity.

3 | Conclusion

We have presented a dispensing-based VAM method that enables high-repeat rate 3D printing by projecting tomographically computed light patterns onto a suspended volume of photocurable resin. This approach eliminates the need for resin vats and mechanical detachment steps, significantly simplifying pre- and post-processing. By controlling the formation and rotation of the pendant volume at the pipette tip, the system achieves printing cycle times of approximately 1 min per structure. Characterization of the suspended geometry provided quantitative insight into the printable region and guided an inverse ray-tracing correction strategy that compensates for optical distortion at the curved air-resin interface. This correction improves the dose distribution throughout the exposed volume and enhances the geometric fidelity of 2.5D and 3D structures, including those containing tips, voids, and holes. The rapid serial printing demonstrations highlight the capability of the method to fabricate a wide range of geometries, including lattices, letter-shaped structures, and freeform models such as the Eiffel and the Thinker, without minimal non-printing delay between prints. These results establish the proposed dispensing-based approach as a streamlined and practical route for high-repeat rate volumetric manufacturing, enabling rapid production of geometrically distinct parts with minimal non-printing overhead. Overall, these results establish DVAM as a practical and robust volumetric manufacturing strategy, enabling rapid, low-overhead fabrication of complex 3D structures with useful and continuously improvable geometric fidelity.

4 | Experimental Section/Methods

4.1 | Photoresin

Diurethane dimethacrylate (DUDMA, Sigma–Aldrich) was mixed at 80:20 wt. % with trimethylolpropane triacrylate (TMPTA, Sigma–Aldrich). Photoinitiator camphorquinone (CQ, Tokyo Chemical Industry) and co-initiator ethyl 4-dimethylaminobenzoate (EDAB, Tokyo Chemical Industry) were added to the resin at a 1:1 ratio by weight. The molar concentration of CQ was 10 mM. The average viscosity of the DUDMA/TMPTA resin is 2000 cP at 20°C, measured by plate and cone geometries (Haake MARS III, ThermoElectron). The penetration depth of DUDMA/TMPTA resin is 1.30 cm at 442 nm wavelength, measured by UV–Vis-NIR spectroscopy (Cary 5000, Agilent). The refractive index of the resin required for the light pattern correction was measured by a digital refractometer (WYA, FAITHFUL instrument). The DUDMA/TMPTA resin is 1.488. The surface tension of the resin was measured using the pendant drop method with a droplet suspended from a 3 mm needle. The droplet shape was captured with a high-resolution camera (aCA4112-20UC, Basler), and the surface tension was determined through pendant drop tensiometry software (https://imagej.net/plugins/pendent-drop). The analysis software uses drop shape analysis to fit the Young-Laplace equation to the drop profile. The surface tension of the DUDMA/TMPTA resin is 32.3 ± 0.4 mN/m.

4.2 | Optical Setup

The optical setup for CAL is depicted in Figure S11. 442 nm UV light from a laser diode (3 W) was coupled into the multimode square fiber (SF, 70 × 70/115/200/400N, CeramOptec) via an objective lens (Lens 1, RMS20X, Thorlabs). The square beam was collimated by an aspheric lens (Lens 2, A397TM-A, Thorlabs) and

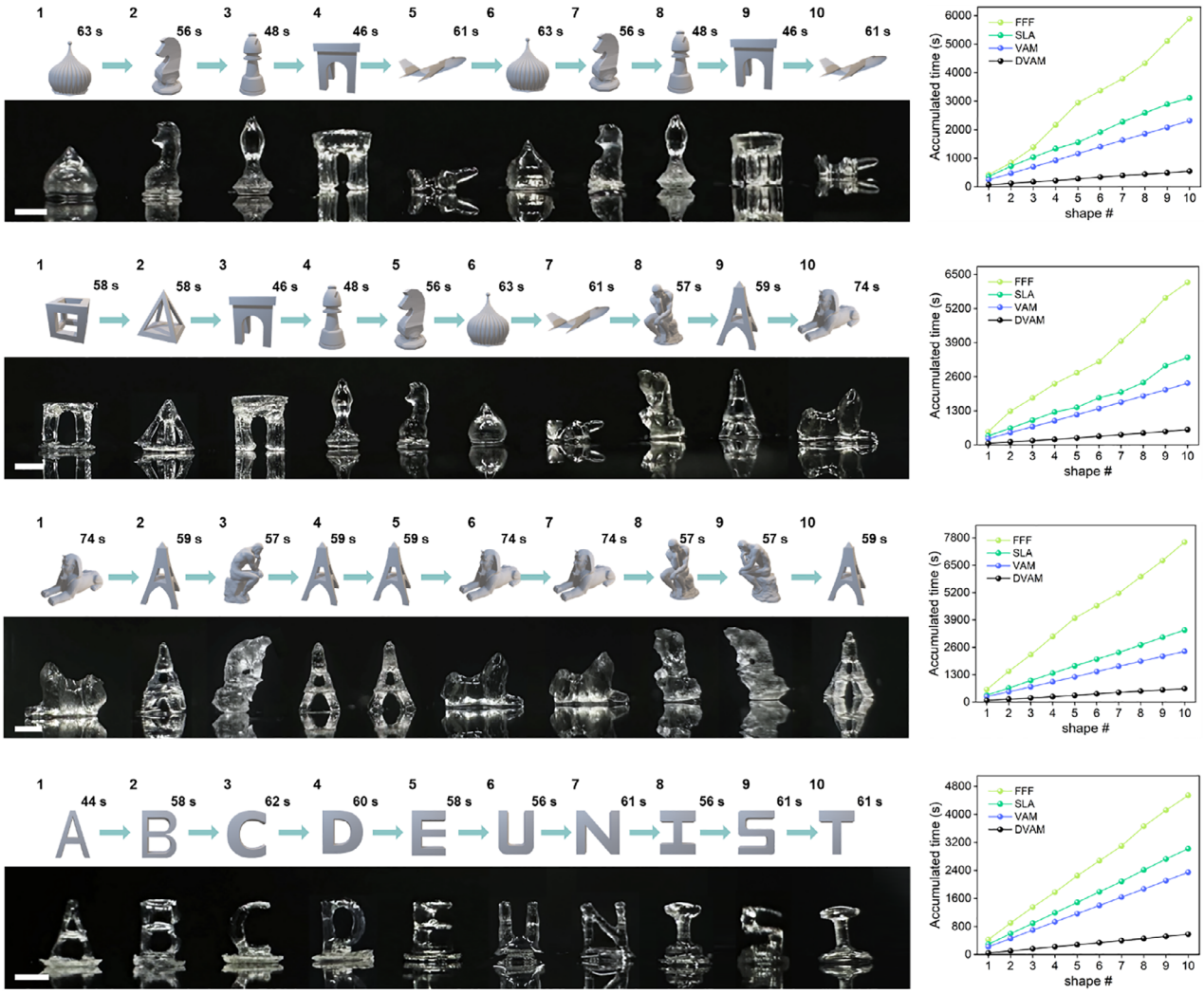

FIGURE 5 | Demonstration of rapid serial volumetric printing for several complex shapes. Each shape exhibits lattice, overhang, or fine features. The printing time is 45–75 s according to each shape, and the non-printing time (dispensing and droplet formation) for the next fabrication is approximately 1–3 s. Each shape is washed as described in the experimental section. They illustrate the reproduction of non-extrudable and freeform shapes. First row: "A B C D E U N I S T" letter. Second row: Basilica dome, Chess knight, Chess bishop, arch, airplane, Basilica dome, Chess knight, Chess bishop, arch, airplane. Third row: cubic lattice, hollow square pyramid, arch, Chess bishop, Chess knight, Basilica dome, groin, airplane, Eiffel, Sphinx. Fourth row: Sphinx, Eiffel, Thinker, Thinker, Eiffel, Eiffel, Sphinx, Sphinx, Thinker, Eiffel. The scale bar is 1 mm. The graphs on the right compare the accumulated total fabrication time (printing + non-printing steps) among FFF, SLA, VAM, and DVAM methods for ten consecutive prints. The DVAM approach exhibits high-repeat rate operation while eliminating intermediate resin replacement and platform building steps.

expanded by a plano-concave lens (Lens 3, LC1054-A, Thorlabs) and a plano-convex lens (Lens 4, LA1433-A, Thorlabs). Light patterns from the DMD (V-9601 VIS, Vialux, 10.8 μm pixel pitch) were projected onto the resin via a plano-convex lens (Lens 5, LA1509-A, Thorlabs) with focal length f = 100 mm and a lever-actuated iris diaphragm (Aperture, SM1D12, Thorlabs). The projected pixel size at the central plane of the resin droplet was 7.45 μm per pixel, as determined by optical calibration. And, three mirrors (BB1-E02, Thorlabs) are used. The photocurable resin was dispensed from the borosilicate glass pipe (OD: 4 mm, ID: 2.4 mm). These pipes were rotated by the motorized precision rotation stage (PRM1Z8, Thorlabs, maximum rotation speed: 25° s^{-1}). The CCD camera (aCA4112-20UC, Basler) performed in situ imaging with an achromatic lens pair; focal length = 75 mm (Lens 6–7, AC508-075-A-ML, Thorlabs) and focal length = 250 mm (Lens 8, AC508-250-A-ML, Thorlabs). The moving substrate is driven by an Arduino-based stepper motor, which transfers the dispensed prints. The resin is exposed to 442 nm light with a maximum intensity of 36 mW cm^{-2}.

4.3 | Post-Processing

All printed objects were transferred out of the washing chamber via the moving substrate and left to rinse in isopropyl alcohol (IPA, Sigma–Aldrich) for 2 min under sonication.

4.4 | Imaging of the Prints

Qualitative and quantitative side- and top-view images were acquired using a high-resolution CMOS camera (a2A4504-18UC,

Basler) under coaxial white LED illumination with a telecentric lens, providing a pixel size of 2.74 μm at the object plane.

4.5 | Measurement of Print Fidelity

Printed objects were also imaged using X-ray micro-CT (VTOMEX M300, Baker Hughes) with a 160 kV and voxel sizes of 4 μm × 4 μm × 4 μm. Image tomography was obtained with VG Studio (HEXAGON). To quantitatively evaluate the volumetric printing accuracy, the 3D image stacks obtained from the Micro-CT were processed and compared with the original CAD designs. The experimental CT data were binarized using the Otsu thresholding method. These 3D image stacks were then spatially aligned with the target CAD models. The alignment (transformation + rotation) was performed using an iterative closest point algorithm prior to IoU computation. The printing fidelity was quantified by calculating the Jaccard Index (Intersection over Union) over the entire 3D volume using Python code.

4.6 | Data Processing and 3D Model

The contact angle and maximum height of the pendant drop, or the feature size of the prints, were also measured using ImageJ software from the captured images. The 3D models were designed using CAD software (Solidworks, Dassault Systèmes) and (3ds Max, Autodesk). Some 3D models were obtained freely from https://www.printables.com/.

Acknowledgements

This work was supported by the National Research Foundation (NRF) grant funded by the Korea government (MSIT) (Nos. RS-2023-00211636, RS-2024-00416891, and RS-2025-2453204), Institute of Information & communications Technology Planning & Evaluation (IITP) grant funded by the Korea government (MSIT) (No. 2020-0-01336, Artificial Intelligence Graduate School Program (UNIST)), and the Human Resources Development of the Korea Institute of Energy Technology Evaluation and Planning (KETEP) grant funded by the Korea government Ministry of Knowledge Economy (No. RS-2023-00240918).

Conflicts of Interest

The authors declare no conflicts of interest.

Data Availability Statement

The data that support the findings of this study are available in the supplementary material of this article.

References

1. E. Seo, Y. N. Lee, W. Y. Shin, et al., "Structural Influence on Titanium Ion Dissolution in 3D-Printed Ti_6Al_4V Orthopedic Implants," *Scientific Reports* 15 (2025): 37122, https://doi.org/10.1038/s41598-025-21129-9.

2. A. D. Valentine, T. A. Busbee, J. W. Boley, et al., "Hybrid 3D Printing of Soft Electronics," *Advanced Materials* 29 (2017): 1703817 , https://doi.org/10.1002/adma.201703817.

3. H. Lee, Z. Wang, Q. Rao, et al., "Additive Manufacturing of Thermoelectric Microdevices for 4D Thermometry," *Advanced Materials* 35 (2023): 2301704, https://doi.org/10.1002/adma.202301704.

4. Y. Kim, H. Yuk, R. Zhao, S. A. Chester, and X. Zhao, "Printing Ferromagnetic Domains For Untethered Fast-Transforming Soft Materials," *Nature* 558 (2018): 274–279, https://doi.org/10.1038/s41586-018-0185-0.

5. Y. Zhai, A. D. Boer, J. Yan, et al., "Desktop Fabrication Of Monolithic Soft Robotic Devices With Embedded Fluidic Control Circuits," *Science Robotics* 8 (2023): 79, https://doi.org/10.1126/scirobotics.adg3792.

6. N. Zhao, M. Parthasarathy, S. Patil, et al., "Direct Additive Manufacturing Of Metal Parts For Automotive Applications," *Journal of Manufacturing Systems* 68 (2023): 368–375, https://doi.org/10.1016/j.jmsy.2023.04.008.

7. E. Sacco and S. Moon, "Additive Manufacturing For Space: Status And Promises," *The International Journal of Advanced Manufacturing Technology* 105 (2019): 4123–4146, https://doi.org/10.1007/s00170-019-03786-z.

8. B. Grigoryan, S. J. Paulsen, D. C. Corbett, et al., "Multivascular Networks And Functional Intravascular Topologies Within Biocompatible Hydrogels," *Science* 364 (2019): 458, https://doi.org/10.1126/science.aav9750.

9. S. H. Kim, Y. K. Yeon, J. M. Lee, et al., "Precisely Printable And Biocompatible Silk Fibroin Bioink For Digital Light Processing 3D Printing," *Nature Communications* 9 (2018): 1620, https://doi.org/10.1038/s41467-018-03759-y.

10. S. B. Gugulothu and K. Chatterjee, "Visible Light-Based 4D-Bioprinted Tissue Scaffold," *ACS Macro Letters* 12 (2023): 494, https://doi.org/10.1021/acsmacrolett.3c00036.

11. M. Yang, L. Chu, Y. Zhuang, et al., "Multi-Material Digital Light Processing (DLP) Bioprinting of Heterogeneous Hydrogel Constructs With Perfusable Networks," *Advanced Functional Materials* 34 (2024): 2316456, https://doi.org/10.1002/adfm.202316456.

12. M. Shusteff, A. E. M. Browar, B. E. Kelly, et al., "One-Step Volumetric Additive Manufacturing Of Complex Polymer Structures," *Science Advances* 3 (2017): 12, https://doi.org/10.1126/sciadv.aao5496.

13. D. J. Whyte, E. H. Doeven, A. Sutti, A. Z. Kouzani, and S. D. Adams, "Volumetric Additive Manufacturing: A New Frontier In Layer-Less 3D Printing," *Additive Manufacturing* 84 (2024): 104094, https://doi.org/10.1016/j.addma.2024.104094.

14. P. N. Bernal, P. Delrot, D. Loterie, et al., "Volumetric Bioprinting of Complex Living-Tissue Constructs Within Seconds," *Advanced Materials* 31 (2019): 1904209, https://doi.org/10.1002/adma.201904209.

15. B. E. Kelly, I. Bhattacharya, H. Heidari, M. Shusteff, C. M. Spadaccini, and H. K. Taylor, "Volumetric Additive Manufacturing Via Tomographic Reconstruction," *Science* 363 (2019): 1075–1079, https://doi.org/10.1126/science.aau7114.

16. M. Kollep, G. Konstantinou, J. Madrid-Wolff, et al., "Tomographic Volumetric Additive Manufacturing of Silicon Oxycarbide Ceramics," *Advanced Engineering Materials* 24 (2022): 2101345, https://doi.org/10.1002/adem.202101345.

17. J. T. Toombs, M. Luitz, C. C. Cook, et al., "Volumetric Additive Manufacturing Of Silica Glass With Microscale Computed Axial Lithography," *Science* 376 (2022): 308–312, https://doi.org/10.1126/science.abm6459.

18. J. J. Schwartz, D. H. Porcincula, C. C. Cook, E. J. Fong, and M. Shusteff, "Volumetric Additive Manufacturing Of Shape Memory Polymers," *Polymer Chemistry* 13 (2022): 1813–1817, https://doi.org/10.1039/D1PY01723C.

19. M. Xie, L. Lian, X. Mu, et al., "Volumetric Additive Manufacturing Of Pristine Silk-Based (bio)Inks," *Nature Communications* 14 (2023): 210, https://doi.org/10.1038/s41467-023-35807-7.

20. W. Qiu, J. Gehlen, M. Bernero, et al., "A Synthetic Dynamic Polyvinyl Alcohol Photoresin for Fast Volumetric Bioprinting of Functional Ultrasoft Hydrogel Constructs," *Advanced Functional Materials* 33 (2023): 2214393, https://doi.org/10.1002/adfm.202214393.

21. A. Orth, D. Webber, Y. Zhang, et al., "Deconvolution Volumetric Additive Manufacturing," *Nature Communications* 14 (2023): 4412, https://doi.org/10.1038/s41467-023-39886-4.

22. D. Loterie, P. Delrot, and C. Moser, "High-Resolution Tomographic Volumetric Additive Manufacturing," *Nature Communications* 11 (2020): 852, https://doi.org/10.1038/s41467-020-14630-4.

23. M. I. Álvarez-Castaño, A. G. Madsen, J. Madrid-Wolff, et al., "Holographic Tomographic Volumetric Additive Manufacturing," *Nature Communications* 16 (2025): 1151, https://doi.org/10.1038/s41467-025-56852-4.

24. M. Regehly, Y. Garmshausen, M. Reuter, et al., "Xolography for Linear Volumetric 3D Printing," *Nature* 588 (2020): 620–624, https://doi.org/10.1038/s41586-020-3029-7.

25. N. F. König, M. Reuter, M. Reuß, et al., "Xolography for 3D Printing in Microgravity," *Advanced Materials* 37 (2025): 2413391, https://doi.org/10.1002/adma.202413391.

26. L. Stoecker, G. Cedillo-Servin, N. F. König, et al., "Xolography for Biomedical Applications: Dual-Color Light-Sheet Printing of Hydrogels With Local Control Over Shape and Stiffness," *Advanced Materials* 37 (2025): 2410292, https://doi.org/10.1002/adma.202410292.

27. D. Dendukuri, D. C. Pregobon, J. Collins, T. A. Hatton, and P. S. Dolye, "Continuous-Flow Lithography For High-Throughput Microparticle Synthesis," *Nature Materials* 5 (2006): 365–369, https://doi.org/10.1038/nmat1617.

28. S.-H. Song, K. Kim, S.-E. Choi, et al., "Fine-Tuned Grayscale Optofluidic Maskless Lithography For Three-Dimensional Freeform Shape Microstructure Fabrication," *Optics Letters* 39 (2014): 5162–5165, https://doi.org/10.1364/OL.39.005162.

29. C.-Y. Wu, K. Owsley, and D. D. Carlo, "Rapid Software-Based Design and Optical Transient Liquid Molding of Microparticles," *Advanced Materials* 27 (2015): 7970–7978, https://doi.org/10.1002/adma.201503308.

30. S. Habasaki, W. C. Lee, S. Yoshida, and S. Takeuchi, "Vertical Flow Lithography for Fabrication of 3D Anisotropic Particles," *Small* 11 (2015): 6391–6396, https://doi.org/10.1002/smll.201502968.

31. K. S. Paulsen, D. D. Carlo, and A. J. Chung, "Optofluidic Fabrication for 3D-Shaped Particles," *Nature Communications* 6 (2015): 6976, https://doi.org/10.1038/ncomms7976.

32. L. Stüwe, M. Geiger, F. Röllgen, et al., "Continuous Volumetric 3D Printing: Xolography in Flow," *Advanced Materials* 36 (2024): 2306716, https://doi.org/10.1002/adma.202306716.

33. P.-H. Tsai and A.-B. Wang, "Classification and Prediction of Dripping Drop Size for a Wide Range of Nozzles by Wetting Diameter," *Langmuir* 35 (2019): 4763–4775, https://doi.org/10.1021/acs.langmuir.8b04228.

34. A. Orth, K. L. Sampson, K. Ting, J. Boisvert, and C. Paquet, "Correcting Ray Distortion In Tomographic Additive Manufacturing," *Optics Express* 29 (2021): 11037–11054, https://doi.org/10.1364/OE.419795.

35. D. Webber, Y. Zhang, M. Picard, J. Boisvert, C. Paquet, and A. Orth, "Versatile Volumetric Additive Manufacturing With 3D Ray Tracing," *Optics Express* 31 (2023): 5531–5546, https://doi.org/10.1364/OE.481318.

36. J. Redmon, S. Divvala, R. Girshick, and A. Farhadi, "You Only Look Once: Unified, Real-Time Object Detection," in *Proceedings of the IEEE Conference on Computer Vision and Pattern Recognition (CVPR)* IEEE, (2016): 779–788, https://doi.org/10.1109/Cvpr.2016.91779.

37. Y. Zhang, H. D. Haan, K. Houlahan, et al., "Impact of Oxygen Inhibition on (meth)Acrylate Photopolymerization In Tomographic Volumetric Printing," *Additive Manufacturing* 109 (2025): 104844, https://doi.org/10.1016/j.addma.2025.104844.

38. R. Salajeghe, D. H. Meile, C. S. Kruse, D. Marla, and J. Spangenberg, "Numerical Modeling Of Part Sedimentation During Volumetric Additive Manufacturing," *Additive Manufacturing* 66 (2023): 103459, https://doi.org/10.1016/j.addma.2023.103459.

Supporting Information

Additional supporting information can be found online in the Supporting Information section.

Supporting File 1: adfm75048-sup-0001-SuppMat.docx.

Supporting File 2: adfm75048-sup-0002-MovieS1.docx.

Supporting File 3: adfm75048-sup-0003-MovieS2.docx.

Supporting File 4: adfm75048-sup-0004-MovieS3.docx.